# Algorithm Development for Land Surface Temperature Retrieval: Application to Chinese Gaofen-5 Data

Yuanyuan Chen, Si-Bo Duan, Huazhong Ren, Jélila Labed, Zhao-Liang Li

*remote sensing*

MDPI

*Article*

# Algorithm Development for Land Surface Temperature Retrieval: Application to Chinese Gaofen-5 Data

**Yuanyuan Chen [1,2], Si-Bo Duan [1], Huazhong Ren [3], Jelila Labed [2] and Zhao-Liang Li [1,2,*]**

[1] Key Laboratory of Agri-informatics, Ministry of Agriculture/Institute of Agricultural Resources and Regional Planning, Chinese Academy of Agricultural Sciences, Beijing 100081, China; cy1305153@163.com (Y.C.); duansibo@caas.cn (S.-B.D.)

[2] ICube (UMR7357), UdS, CNRS, 300 Bld Sébastien Brant, CS10413, Illkirch 67412, France; Labed@unistra.fr

[3] Institute of Remote Sensing and Geographic Information System, School of Earth and Space Sciences, Peking University, Beijing 100871, China; renhuazhong@pku.edu.cn

* Correspondence: lizhaoliang@caas.cn; Tel.: +86-10-8210-5077

Academic Editors: Jose Moreno and Prasad S. Thenkabail

Received: 7 December 2016; Accepted: 13 February 2017; Published: 16 February 2017

**Abstract:** Land surface temperature (LST) is a key variable in the study of the energy exchange between the land surface and the atmosphere. Among the different methods proposed to estimate LST, the quadratic split-window (SW) method has achieved considerable popularity. This method works well when the emissivities are high in both channels. Unfortunately, it performs poorly for low land surface emissivities (LSEs). To solve this problem, assuming that the LSE is known, the constant in the quadratic SW method was calculated by maintaining the other coefficients the same as those obtained for the black body condition. This procedure permits transfer of the emissivity effect to the constant. The result demonstrated that the constant was influenced by both atmospheric water vapour content (W) and atmospheric temperature ($T_0$) in the bottom layer. To parameterize the constant, an exponential approximation between W and $T_0$ was used. A LST retrieval algorithm was proposed. The error for the proposed algorithm was RMSE = 0.70 K. Sensitivity analysis results showed that under the consideration of NE$\Delta$T = 0.2 K, 20% uncertainty in W and 1% uncertainties in the channel mean emissivity and the channel emissivity difference, the RMSE was 1.29 K. Compared with AST 08 product, the proposed algorithm underestimated LST by about 0.8 K for both study areas when ASTER L1B data was used as a proxy of Gaofen-5 (GF-5) satellite data. The GF-5 satellite is scheduled to be launched in 2017.

**Keywords:** land surface temperature; land surface emissivity; split-window; Gaofen-5

## 1. Introduction

As a key parameter of the surface energy budget, land surface temperature (LST) is directly related to surface energy fluxes and to the latent heat flux (evapotranspiration) and water stress in particular [1,2]. The LST is crucial for estimating the net radiation driven by the surface longwave emission [3] and for computing soil moisture [4,5]. Moreover, LST is an essential climate variable for understanding meteorological and hydrological processes in a changing climate [6–8]. Thus, understanding and monitoring the dynamics of the LST is critical for modelling and predicting climate and environmental changes and for other applications such as agriculture, urban heat island and vegetation monitoring [9–12].

The Chinese Gaofen-5 (GF-5) satellite is expected to be launched in 2017. One of its missions is to collect land information at high spatial resolution from visible to thermal infrared (TIR) spectral

range for performing disaster monitoring. The multiple spectral-imager (MSI) is a payload onboard this satellite and has a 40-m spatial resolution for TIR channels. Development of a suitable algorithm for retrieving LST from the GF-5 data is urgently needed.

Remote sensing is a more effective method to map LST at large temporal and spatial scales than traditional measurement. However, accurate determination of the LST from satellite data is a difficult task because it is necessary to correct the remote sensing measurements for atmospheric absorption and emission and for the effect of surface emissivity, the latter generally differing from unity and being channel dependent [13]. Efforts have been devoted to estimating LST from satellite measurements [14–19]. A complete review of different LST retrieval methods can be found in the literature [20].

The selection of the LST algorithm for GF-5 data is based on a literature review and the characteristics of the GF-5 satellite data. The single-window method requires high-quality atmospheric profile and is sensitive to uncertainties in the atmospheric corrections. Considering the simultaneous retrieval of the LST and the land surface emissivity (LSE), the temperature and emissivity separation (TES) method may be a candidate. However, significant errors in the LST and LSE for the surfaces with low spectral contrast emissivity (e.g., water, snow, vegetation) can be caused by the TES [21,22]. Since the GF-5 satellite observes the land almost at nadir, the dual-angle algorithm was discarded. Among the various methods proposed for LST determination, the quadratic split-window (SW) algorithm has received considerable attention because of its simplicity. It can be written as [13,15]:

$$T_s = T_i + A(T_i - T_j)^2 + B(T_i - T_j) + C \quad (1)$$

where $T_s$ is the land surface temperature (LST), $T_i$ and $T_j$ are the at-sensor brightness temperatures for two TIR channels, $A$ and $B$ are coefficients and $C$ is a constant. To correct the emissivity effect, different parameterizations of $A$, $B$ and $C$ can be found in the literature: (i) Constant $C$ was formulated as a function of the mean ($\varepsilon = (\varepsilon_i + \varepsilon_j)/2$) and difference ($\Delta\varepsilon = \varepsilon_i - \varepsilon_j$) of the two channel LSEs, keeping the other coefficients independent of LSE as in sea surface temperature (SST) retrieval [23]. (ii) To make Equation (1) applicable to more general atmospheric conditions, Sobrino and Raissouni proposed modifying constant $C$ as the linear combination of $\varepsilon$, $\Delta\varepsilon$ and atmospheric water vapour content (W) [24]. (iii) Assuming $\Delta\varepsilon = 0$, François and Ottlé presented different coefficients for different $\varepsilon$ values [25]. (iv) Sun and Pinker addressed the SW coefficients according to different surface types to account for LSE effect [26]. It should be noted that the land surface is complex and that the LSE may be quite different from unity and depends on the channel [27]. Considering the effect of the emissivity, the quadratic SW algorithm may not work well. As François and Ottlé noted in their work, when $\varepsilon$ is greater than 0.95, good accuracy can be obtained using the quadratic method with the emissivity-dependent coefficients. That means, when $\varepsilon$ is low, the quadratic relationship no longer performs well or is changed. Therefore, the quadratic method should be re-examined and improved, especially for low emissivity.

This study aims to improve the quadratic SW method and develop a LST algorithm for GF-5 data. The variation in the channel emissivity will be also considered, which was not checked in the study by François and Ottlé. The paper is organized as follows: Section 2 describes the data used in this study. The algorithm development is documented in Section 3. Section 4 presents the results using the simulated data and the sensitivity of the developed algorithm to the uncertainties of the input parameters is also analysed in this Section. The operational application of the algorithm to the satellite data is given in Section 5. Section 6 discusses the developed algorithm. Finally, Section 7 describes the conclusions.

## 2. Data

### *2.1. Chinese GF-5 Data*

GF-5 is the fifth satellite of a series of China High-resolution Earth Observation System (CHEOS) satellites of the China National Space Administration (CNSA) and is scheduled to be launched in 2017. One sensor onboard the GF-5 satellite is the MSI, which includes 13 channels covering the spectral range from visible to TIR. Two TIR channels suitable for the SW method are designed to be centred at 10.8 μm and 11.95 μm ($CH_{10.8}$ and $CH_{11.95}$, respectively) with a resolution of 40 m. The spectral response functions of these two channels are displayed in Figure 1. The MSI has a narrow swath (60 km) and observes the land almost at nadir.

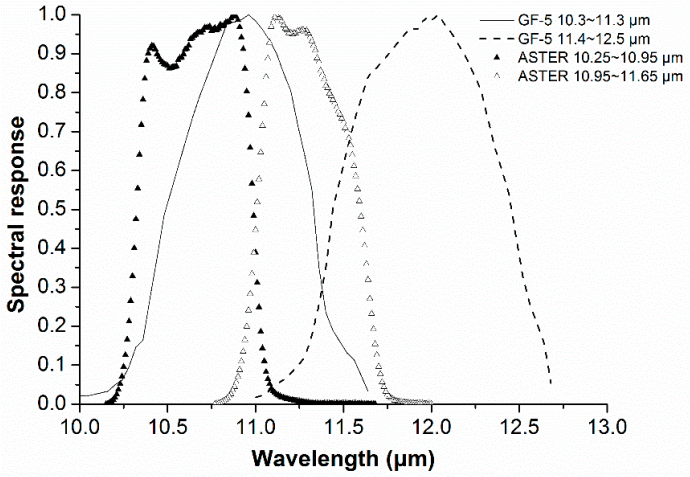


**Figure 1.** Spectral response functions of the GF-5 and ASTER split-window channels.

### *2.2. ASTER Data*

The Advanced Spaceborne Thermal Emission and Reflection Radiometer (ASTER) is a sensor on NASA Earth Observing System (EOS) Terra satellite. ASTER is capable of creating detailed land information, with four 15-m visible near-infrared (NIR) bands, including stereo, six 30-m shortwave infrared (SWIR) bands and five 90-m TIR bands. The central wavelengths of two TIR bands, which are suitable for SW method, are 10.657 μm and 11.318 μm. The spectral response functions for these two SW channels are shown in Figure 1. The noise equivalent differential temperature (NE$\Delta$T) at 300 K is $\leq$ 0.3 K. ASTER L1B is the registered radiance data. AST 05 and AST 08 are the standard emissivity and temperature products, generated using the TES algorithm. The numerical simulation and some field experiments has evaluated the accuracy of AST 05 and AST 08 to be within $\pm$0.015 and $\pm$1.5 K [18]. The ASTER L1B data was used as a proxy for evaluating the performance of the developed LST retrieval algorithm. AST 05 was used as the emissivity input and AST 08 was for the inter-comparison purpose to assess the retrieved LST using the developed algorithm.

### *2.3. MOD 05 Data*

The Moderate-resolution Imaging Spectroradiometer (MODIS) is another instrument on Terra satellite. MOD 05 Level 2 is a precipitable water product generated by the NIR algorithm during the day at 1-km spatial resolution and by infrared algorithm both day and night at 5-km resolution. The infrared column water vapor parameter was derived by integrating the moisture profile through the atmospheric column or by SW method. The data quality of MOD 05 is guaranteed by performing comparisons of specific validation sites across as many different climatic and geographic regions as possible. The MOD 05 Level 2 was used as the source of water vapour input for the LST retrieval algorithm.

### 2.4. Atmospheric Profile Data

The Thermodynamic Initial Guess Retrieval (TIGR) database has been widely used for development of LST retrieval algorithms [28]. In this work, we chose the TIGR database TIGR2002_v1.1 as the atmospheric data to execute the radiative transfer simulation procedure (see Section 2.5). However, it was found that TIGR2002_v1.1 is centred at low W values of less than 1.0 g/cm$^2$. To obtain robust statistics, it is necessary to select different atmospheric profiles to make W uniformly distributed from dry to moist. Figure 2 shows the selected 126 atmospheric profiles in which the atmospheric temperature ($T_0$) in the lowest layer varies from 232.25 K to 311.95 K and W varies from 0.09 g/cm$^2$ to 6.15 g/cm$^2$, which represent worldwide atmospheric conditions with a moderate sample number and ensure that there is a nearly uniform distribution for W. Ninety-eight profiles (referred to as TIGR_98) were used for development of the LST retrieval algorithm and twenty-eight (referred to as TIGR_28) were used for validation.

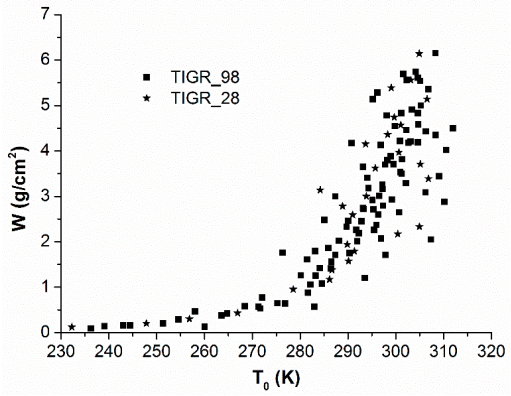


**Figure 2.** Plot of the total water vapour content (W) versus bottom layer atmospheric temperature ($T_0$) for the selected atmospheres. TIGR_98 were used for algorithm development, and TIGR_28 were used for algorithm validation.

### 2.5. Generation of the Simulation Database

The radiative transfer equation (RTE), which is the basis for determining LST, gives the radiance measured from the sensor in channel *i* for the cloud-free atmosphere:

$$B_i(T_i) = \varepsilon_i B_i(T_s)\tau_i + R^{\uparrow}_{atm\_i} + (1-\varepsilon_i)R^{\downarrow}_{atm\_i}\tau_i \quad (2)$$

where $B_i$ is the Planck function, $\varepsilon_i$ is the channel emissivity, $\tau_i$ is the total atmospheric transmittance along the target-to-sensor path, $R^{\uparrow}_{atm\_i}$ is the thermal-path atmospheric upwelling radiance and $R^{\downarrow}_{atm\_i}$ is the atmospheric downwelling radiance from the entire hemisphere divided by $\pi$.

To obtain an appropriate simulation database for developing the LST retrieval algorithm for GF-5 TIR data, the atmospheric radiative transfer model MODTRAN 4 [29] was used to simulate the spectral atmospheric parameters of spectral transmittance $\tau_\lambda$, spectral atmospheric upwelling radiance $R^{\uparrow}_{atm\_\lambda}$ and spectral atmospheric downwelling radiance $R^{\downarrow}_{atm\_\lambda}$. The channel-effective atmospheric parameters $\tau_i$, $R^{\uparrow}_{atm\_i}$ and $R^{\downarrow}_{atm\_i}$ in the RTE can be obtained by convoluting the spectral variables output by MODTRAN with the spectral response functions of $CH_{10.8}$ and $CH_{11.95}$. The channel brightness temperatures at the top of the atmosphere (TOA) can then be determined according to the RTE by inverting the Planck function. For a realistic simulation, the LSTs reasonably vary with the $T_0$ of each profile: from $T_0 - 5$ K to $T_0 + 15$ K in step of 5 K for $T_0 > 280$ K and from $T_0 - 5$ K to $T_0 + 5$ K in step of 5 K for $T_0 \leq 280$ K. Moreover, the channel emissivities $\varepsilon_{10.8}$ and $\varepsilon_{11.95}$ were calculated based on 65 spectrum samples of soil, vegetation, water, ice, and snow from the Johns Hopkins University (JHU) and the Jet Propulsion Laboratory (JPL). According to the ranges of $\varepsilon$ and $\Delta\varepsilon$ shown in Figure 3, $\varepsilon$ is assumed to vary from 0.90 to 1 with a 0.02 interval and $\Delta\varepsilon$ varies from $-0.02$

to 0.03 with a 0.005 interval. Because the MSI onboard the GF-5 satellite observes the land almost at nadir, it is reasonable to ignore the viewing zenith angle variation. A flow chart of simulation data generation is shown in Figure 4.

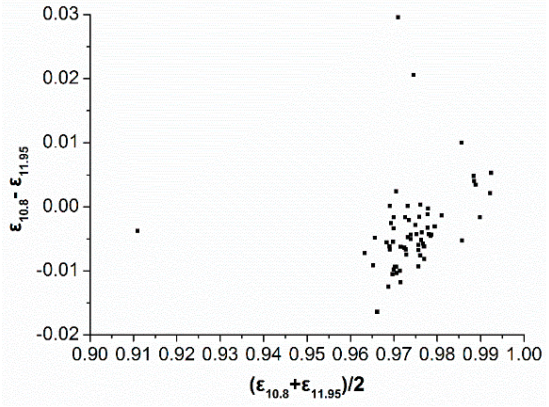


**Figure 3.** Scatter plot of the channel mean emissivity $(\varepsilon_{10.8} + \varepsilon_{11.95})/2$ and channel emissivity difference $(\varepsilon_{10.8} - \varepsilon_{11.95})$.

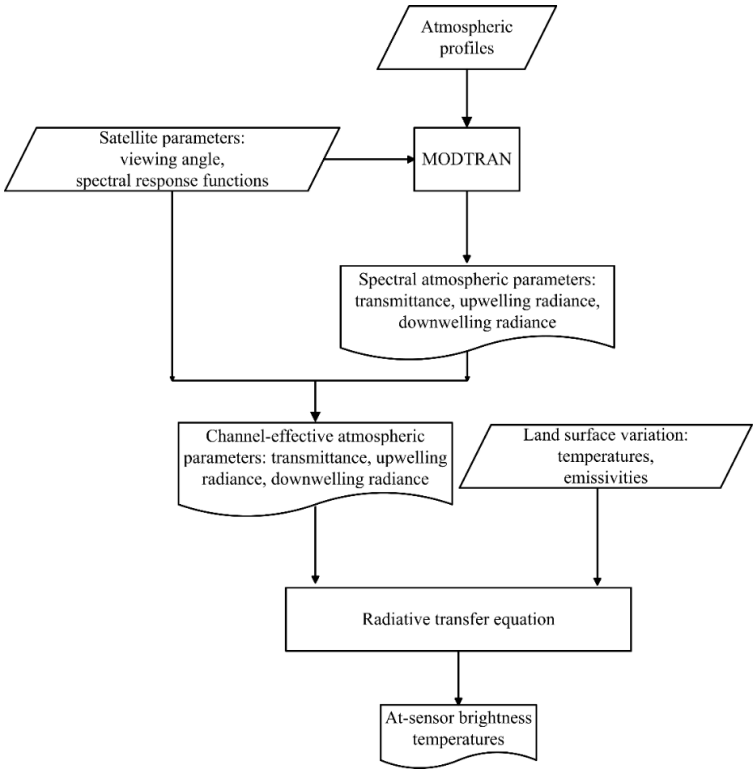


**Figure 4.** The procedure for generating the simulation data.

## 3. Algorithm Development

Using Equation (1), the dependence of $T_s - T_i$ on $T_i - T_j$ was examined for each combination of $\varepsilon$ and $\Delta\varepsilon$. For this purpose, the TOA $T_{10.8}$ and $T_{11.95}$ for two GF-5/TIR channels were simulated. Figure 5 demonstrates that the variation in the emissivity deteriorates the quadratic relationship between $T_s - T_i$ and $T_i - T_j$, taking the combinations of (a) $\varepsilon = 0.90$ and $\Delta\varepsilon = -0.02$, (b) $\varepsilon = 0.90$ and $\Delta\varepsilon = 0$, (c) $\varepsilon = 0.98$ and $\Delta\varepsilon = -0.02$ and (d) $\varepsilon = 0.98$ and $\Delta\varepsilon = 0$ as examples. Figure 5 confirms that Equation (1) works well for case (d). For smaller $\varepsilon$, the quadratic relationship is deteriorated for $\Delta\varepsilon$ of

0 and −0.02. Furthermore, Δε of −0.02 tends to intensify this deterioration. Therefore, Equation (1) would lead to large error for low emissivity, especially for the case of (a).

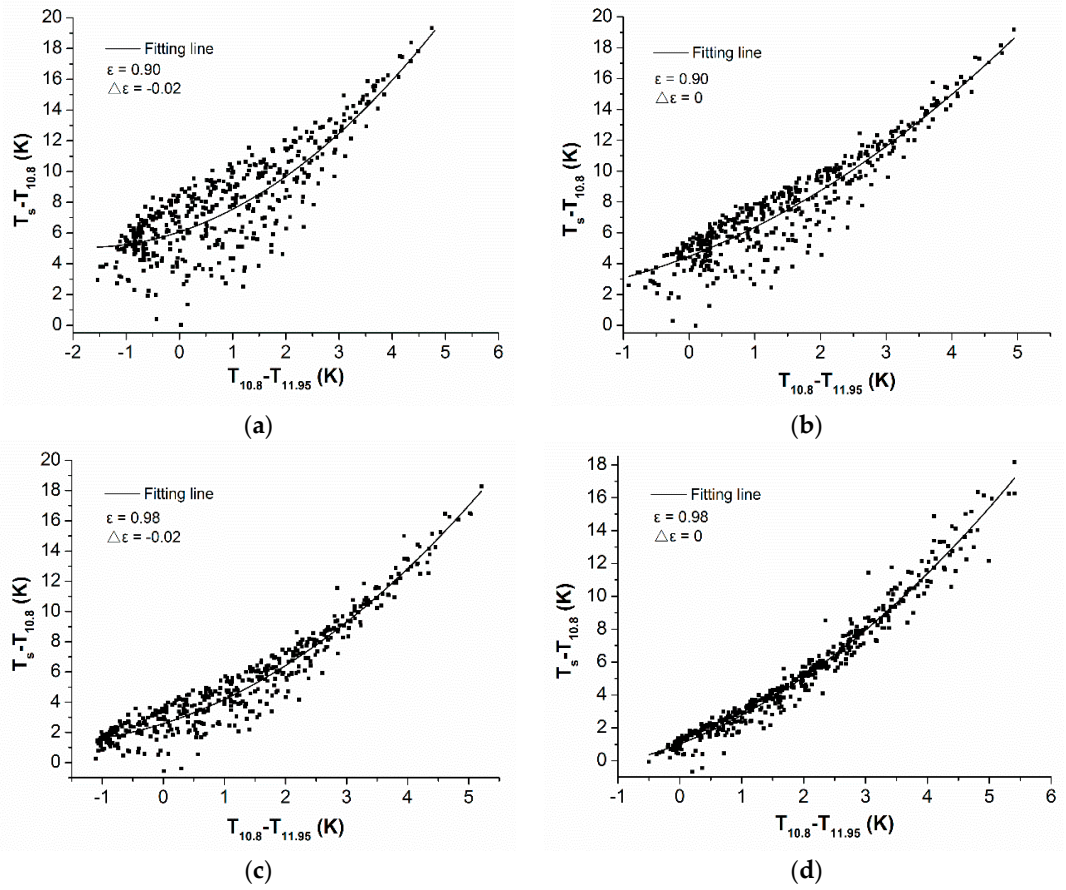


**Figure 5.** Variations of $(T_s - T_{10.8})$ versus $(T_{10.8} - T_{11.95})$ for the emissivity combinations of (**a**) ε = 0.90 and Δε = −0.02, (**b**) ε = 0.90 and Δε = 0, (**c**) ε = 0.98 and Δε = −0.02 and (**d**) ε = 0.98 and Δε = 0. Here, ε is the mean emissivity of the two channels and Δε denotes the emissivity difference.

Assuming $\varepsilon_{10.8} = \varepsilon_{11.95} = 1$, Equation (1) yields $A = 0.2809$, $B = 1.447$ and $C = 0.17$, with RMSE = 0.68 K. Figure 6 is the plot of residual for the black body case, implying the applicability of Equation (1) for SST retrieval. For LST estimation, Coll [15] has shown that the SW coefficients for SST can be used for LST retrieval if the emissivity effect is estimated. Therefore, we used the same $A$ and $B$ to develop the LST algorithm but modified $C$ to correct the emissivity effect.

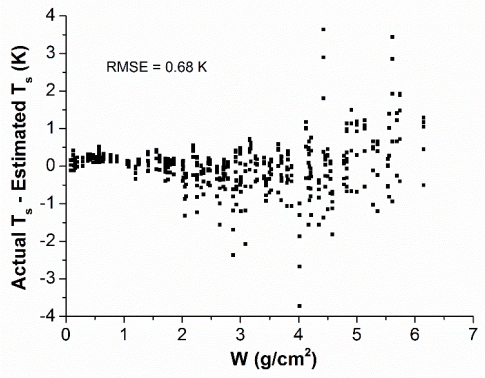


**Figure 6.** The residual yielded by Equation (1) for a black body. Here, W is the water vapour content.

Considering the worst performance of Equation (1) shown in Figure 5a, constant $C$ in Equation (1) was investigated by maintaining coefficients $A$ and $B$ as 0.2809 and 1.447, respectively. It can be seen from Figure 7 that constant $C$ displays a regular variation trend. For atmospheric profiles of W < 1 g/cm$^2$, $C$ ranges from approximately 5 K to 9 K and increases with W. To parameterize $C$, the linear dependence on W can be used. For atmospheres of W > 1 g/cm$^2$, a larger range (approximately 0~9 K) was obtained, and the linear dependence on W appears to be unsatisfactory to parameterize $C$. To explain the regularity of $C$ for W > 1 g/cm$^2$, Figure 8 was produced. For a given surface-air temperature difference $T_s - T_0$, constant $C$ displays a linear dependence on W. The slope and intercept of each linear relationship are listed in Table 1. As seen from Table 1, although both the slope and intercept vary with $T_s - T_0$, when the intercept is fixed using the mean of 8.73, the slope can be approximated by the linear function of $T_s - T_0$, with a RMSE of 0.054 (Figure 9). Based on these analyses, constant $C$ can be written as:

$$C = C_m W + C_n, \text{ if W } < 1 \text{ g/cm}^2 \quad (3)$$

$$C = C_1 W + C_2 = [C_{11}(T_s - T_0) + C_{12}]W + C_2, \text{ if W } > 1 \text{ g/cm}^2 \quad (4)$$

where $C_m$ = 2.63, $C_n$ = 5.56, $C_{11}$ = 0.0485, $C_{12}$ = −1.10 and $C_2$ = 8.73.

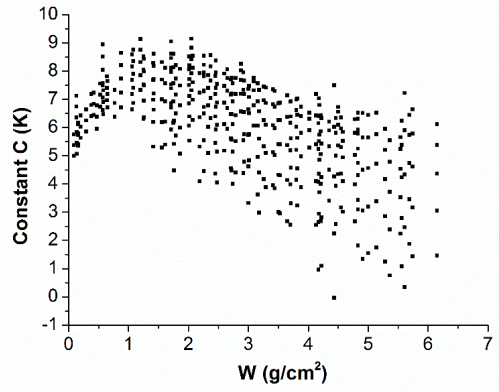


**Figure 7.** Constant $C$ in Equation (1) versus the water vapour content (W), considering a channel mean emissivity of 0.90 and an emissivity difference of −0.02. Coefficients $A$ and $B$ in Equation (1) were set to 0.2809 and 1.447, respectively, obtained for a black body.

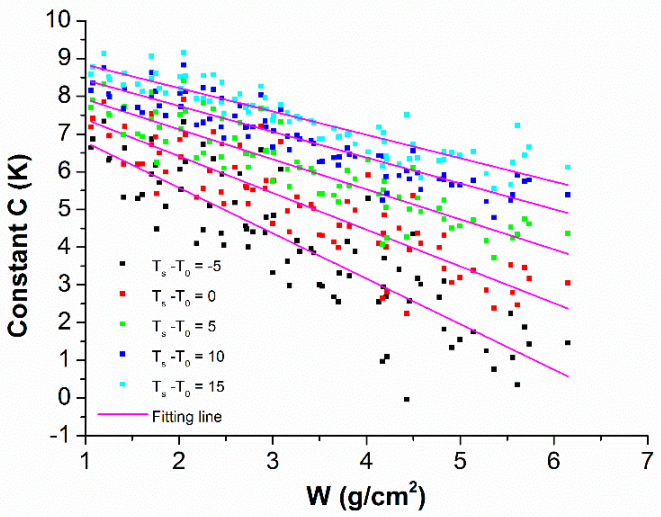


**Figure 8.** For water vapour content (W) greater than 1 g/cm$^2$, constant $C$ in Equation (1) as a function of W for a given surface-air temperature difference $T_s - T_0$.

**Table 1.** For water vapour content (W) greater than 1 g/cm$^2$, the slope and intercept of the linear relationship between constant *C* in Equation (1) and W for a given surface-air temperature difference $T_s - T_0$.

| $T_s - T_0$ (K) | Slope | Intercept |
|---|---|---|
| −5 | −1.205 | 7.99 |
| 0 | −0.974 | 8.36 |
| 5 | −0.795 | 8.72 |
| 10 | −0.684 | 9.11 |
| 15 | −0.620 | 9.46 |

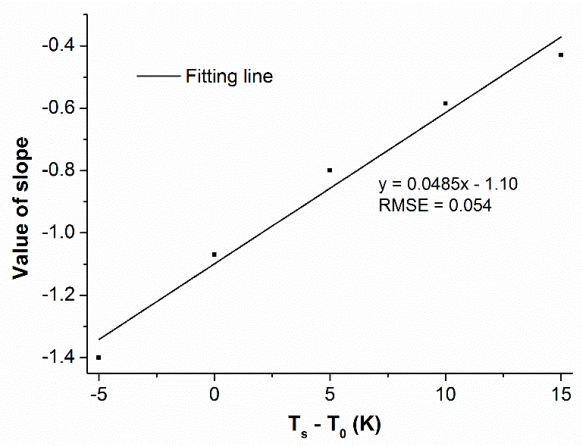


**Figure 9.** For water vapour content (W) greater than 1 g/cm$^2$, the slope of the fitting line between constant *C* in Equation (1) and W versus the surface-air temperature difference $T_s - T_0$.

Because of the difficulties in obtaining atmospheric information, the parameter $T_0$ used in Equation (4) should be eliminated. According to the scatter plot between $W$ and $T_0$ in Figure 2, $W$ can be approximated using an exponential function of $T_0$:

$$W = \alpha e^{\beta T_0} \tag{5}$$

where $\alpha = 2 \times 10^{-7}$ and $\beta = 0.0559$. The fitting error on W is RMSE = 1.05 g/cm$^2$. Inverting Equation (5) yields:

$$T_0 = \frac{\ln W}{\beta} - \frac{\ln \alpha}{\beta} \tag{6}$$

Inserting Equation (6) into Equation (4) yields:

$$C = C_{11} T_s W - \frac{C_{11}}{\beta} \ln(W) W + (C_{11} \frac{\ln \alpha}{\beta} + C_{12}) W + C_2 \tag{7}$$

Because the terms $-\frac{C_{11}}{\beta} \ln(W) W$ and $(C_{11} \frac{\ln \alpha}{\beta} + C_{12}) W$ are both included in Equation (7), the dependence of $-\frac{C_{11}}{\beta} \ln(W) W$ on $W$ was investigated as shown in Figure 10, with a RMSE of 0.04 K. Therefore, Equation (7) can be expressed as:

$$C = C_{11} T_s W + C_a W^2 + C_b W + C_c \tag{8}$$

where $C_a = -0.1357$, $C_b = -0.958 + C_{11} \frac{\ln \alpha}{\beta} + C_{12} = -15.441$ and $C_c = 1.22 + C_2 = 9.95$.

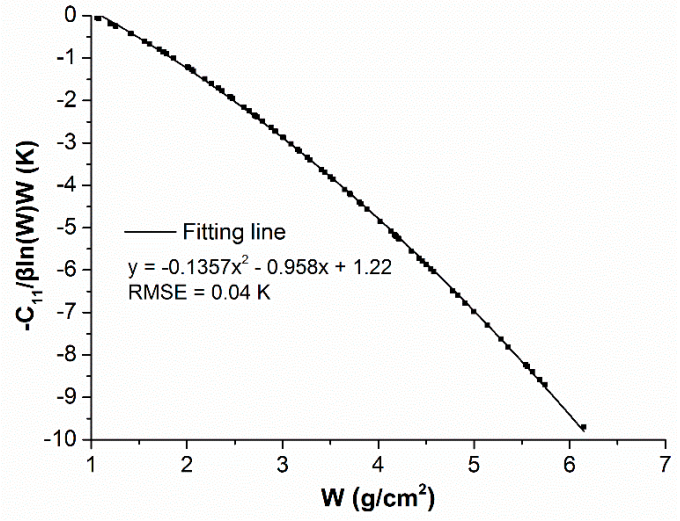


**Figure 10.** Plot of $-C_{11}/\beta \ln(W)W$ in Equation (7) versus W (W: atmospheric water vapour content).

The residual of constant *C* calculated by Equation (3) for W < 1 g/cm$^2$ and by Equation (8) for W > 1 g/cm$^2$ is shown in Figure 11, with RMSE = 0.86 K.

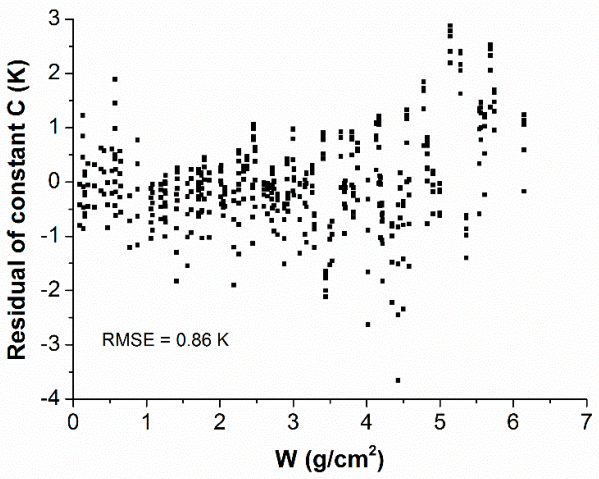


**Figure 11.** The residual of constant *C* calculated using Equation (3) for W < 1 g/cm$^2$ and using Equation (8) for W > 1 g/cm$^2$.

Substituting constant *C* into Equation (1) using Equations (3) and (8), $T_s$ can be estimated using Equations (9) and (10) for a given LSE:

$$T_s = T_{10.8} + A(T_{10.8} - T_{11.95})^2 + B(T_{10.8} - T_{11.95}) + C_m W + C_n, \text{ if W } < 1 \text{ g/cm}^2 \quad (9)$$

$$T_s = \frac{T_{10.8} + A(T_{10.8} - T_{11.95})^2 + B(T_{10.8} - T_{11.95}) + C_a W^2 + C_b W + C_c}{1 - C_{11} W}, \text{ if W } > 1 \text{ g/cm}^2 \quad (10)$$

To obtain stable retrieval accuracy for atmospheres with a *W* of about 1 g/cm$^2$, *W* was divided into two groups with an overlap of 0.4 g/cm$^2$, 0–1.2 and 0.8–6.5 g/cm$^2$, when the least-square fitting method was used to obtain the coefficients in Equations (9) and (10). Table 2 lists coefficients $C_m$ and $C_n$ in Equation (9) and $C_{11}$, $C_a$, $C_b$, and $C_c$ in Equation (10) for the emissivity combinations presented in Figure 5, with $A$ = 0.2809 and $B$ = 1.447. To compare the results, the coefficients and constant in Equation (1) for the same emissivity combinations are shown in Table 3.

**Table 2.** $C_m$ and $C_n$ in Equation (9) and $C_{11}$, $C_a$, $C_b$ and $C_c$ in Equation (10) for different emissivity combinations.

| Emissivity Combinations | Equation (9) | | Equation (10) | | | |
|---|---|---|---|---|---|---|
| | $C_m$ | $C_n$ | $C_{11}$ | $C_a$ | $C_b$ | $C_c$ |
| $\varepsilon = 0.90, \Delta\varepsilon = -0.02$ | 2.131 | 5.74 | 0.03541 | −0.0006 | −12.002 | 9.97 |
| $\varepsilon = 0.90, \Delta\varepsilon = 0$ | 1.699 | 4.13 | 0.02454 | 0.0136 | −8.369 | 7.38 |
| $\varepsilon = 0.98, \Delta\varepsilon = -0.02$ | 0.955 | 2.48 | 0.01695 | 0.0682 | −6.150 | 4.88 |
| $\varepsilon = 0.98, \Delta\varepsilon = 0$ | 0.266 | 1.11 | 0.00404 | 0.1037 | −1.998 | 2.25 |

$\varepsilon$: channel mean emissivity and $\triangle\varepsilon$: channel emissivity difference.

**Table 3.** $A$, $B$ and $C$ in Equation (1) for different emissivity combinations.

| Emissivity Combinations | $A$ | $B$ | $C$ |
|---|---|---|---|
| $\varepsilon = 0.90, \Delta\varepsilon = -0.02$ | 0.3308 | 1.178 | 6.09 |
| $\varepsilon = 0.90, \Delta\varepsilon = 0$ | 0.2463 | 1.641 | 4.47 |
| $\varepsilon = 0.98, \Delta\varepsilon = -0.02$ | 0.3222 | 1.274 | 2.58 |
| $\varepsilon = 0.98, \Delta\varepsilon = 0$ | 0.2823 | 1.462 | 1.03 |

$\varepsilon$: channel mean emissivity and $\triangle\varepsilon$: channel emissivity difference.

In Equations (9) and (10), the coefficients are dependent on the emissivity. Consistent with previous works [23,24,30,31], $(1-\varepsilon)$ and $\Delta\varepsilon$ were used to express coefficients $C_m$, $C_n$, $C_{11}$, $C_a$, $C_b$ and $C_c$ because these six coefficients were generated based on the analysis of the emissivity effect on LST retrieval. Then, Equations (11) and (12) can be obtained:

$$T_s = T_{10.8} + A(T_{10.8} - T_{11.95})^2 + B(T_{10.8} - T_{11.95}) + (C_{m1}(1-\varepsilon) + C_{m2}\Delta\varepsilon)W + C_{n1}(1-\varepsilon) + C_{n2}\Delta\varepsilon + C_o, \text{ if W } < 1\ \text{g/cm}^2 \quad (11)$$

$$T_s = \frac{T_{10.8} + A(T_{10.8} - T_{11.95})^2 + B(T_{10.8} - T_{11.95}) + [C_{a1}(1-\varepsilon) + C_{a2}\Delta\varepsilon]W^2}{1 - [C_{111}(1-\varepsilon) + C_{112}\Delta\varepsilon]W} + \frac{[C_{b1}(1-\varepsilon) + C_{b2}\Delta\varepsilon]W + C_{c1}(1-\varepsilon) + C_{c2}\Delta\varepsilon + C_d}{1 - [C_{111}(1-\varepsilon) + C_{112}\Delta\varepsilon]W}, \text{ if W } > 1\ \text{g/cm}^2 \quad (12)$$

Using the regression for the $W$ groups of 0–1.2 and 0.8–6.5 g/cm$^2$, the coefficients in Equations (11) and (12) were obtained and are shown in Table 4.

**Table 4.** Coefficients in Equations (11) and (12).

| Equations (11) | | Equations (12) | |
|---|---|---|---|
| $A$ | 0.2809 | $A$ | 0.2809 |
| $B$ | 1.447 | $B$ | 1.447 |
| | | $C_{111}$ | 0.2331 |
| | | $C_{112}$ | −0.6917 |
| | | $C_{a1}$ | 0.414 |
| | | $C_{a2}$ | 0.55 |
| $C_{m1}$ | 16.36 | $C_{b1}$ | −80.85 |
| $C_{m2}$ | −33 | $C_{b2}$ | 234.5 |
| $C_{n1}$ | 37.9 | $C_{c1}$ | 71.9 |
| $C_{n2}$ | −92 | $C_{c2}$ | −163 |
| $C_o$ | 0.18 | $C_d$ | 0.09 |

## 4. Results and Sensitivity Analysis

### *4.1. Results*

Using the coefficients in Table 4, the RMSE of 0.70 K is obtained. The residual of LST retrieval using Equations (11) and (12) is shown in Figure 12a. To evaluate the performance of Equations (11) and (12),

the algorithm with W developed by Sobrino and Raissouni (called Sobrino's algorithm) based on the quadratic SW method was used for comparison. Sobrino's algorithm is given in Equation (13) [24]:

$$T_s = T_{10.8} + A(T_{10.8} - T_{11.95})^2 + B(T_{10.8} - T_{11.95}) + (C_{\alpha 1} + C_{\alpha 2}W)(1 - \varepsilon) + (C_{\beta 1} + C_{\beta 2}W)\Delta\varepsilon + C_\gamma \quad (13)$$

Using our simulation data, the coefficients are $A$ = 0.2809, $B$ =1.447, $C_{\alpha 1}$ = 53.8, $C_{\alpha 2}$ = −3.15, $C_{\beta 1}$ = −129, $C_{\beta 2}$ = 16.7 and $C_\gamma$ = 0.10. The residual yielded by Sobrino's algorithm is shown in Figure 12b, with a RMSE of 0.88 K. Comparing Figure 12a,b, we can see that most of the errors yielded by Equations (11) and (12) are less than those by Equation (13). According to the statistical results, 87.7% of the errors between the true and estimated LST using Equations (11) and (12) are within ± 1 K and 80.2% of the errors using Equation (13) are within ± 1 K.

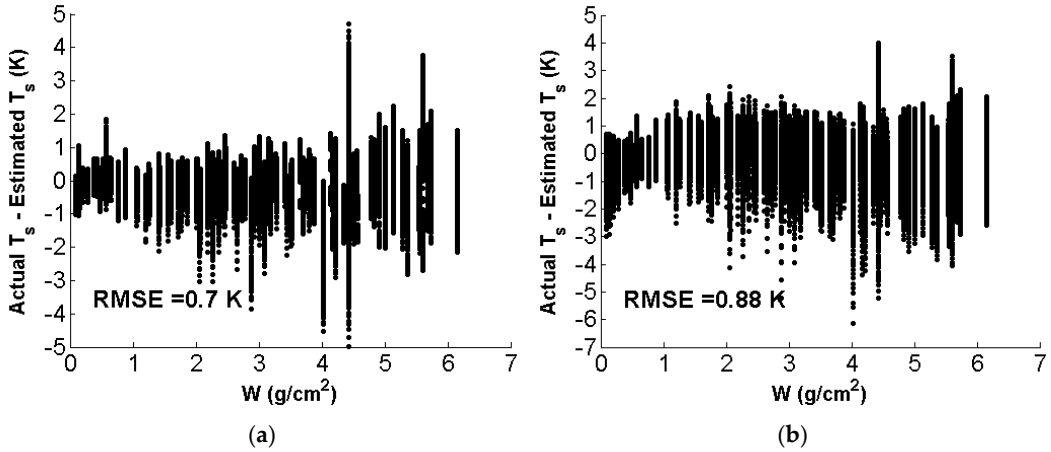


**Figure 12.** The error distributions for (**a**) the algorithm in this study and (**b**) Sobrino's algorithm.

Regarding the results for the given emissivities, such as the emissivity combinations presented in Figure 5, the residuals calculated using Equations (1), (9) and (10) are displayed in Figure 13. When ε = 0.90, Equations (9) and (10) yielded smaller residual ranges and better RMSEs for both Δε of −0.02 and 0. For ε = 0.98, the improvement of Equations (9) and (10) in the residual ranges and RMSEs is not as obvious as for ε = 0.90. This feature can also be seen in Figure 14, which shows the RMSE variations obtained by Equations (1), (9), (10) and (13), with ε = 0.90, 0.94 and 0.98 and Δε = −0.02, 0 and 0.03. Figure 14 clearly demonstrates the following: (i) For low ε, i.e., less than 0.94, the RMSEs obtained using both Equations (1) and (13) decrease as Δε increases. Equations (9) and (10) yield best result for Δε = 0. (ii) For ε = 0.94, Equations (9) and (10) give obviously lower RMSE for all Δε cases, compared with Equation (1). While in comparison with Equation (13), Equations (9) and (10) gives similar RMSE for Δε = 0.03. All these three methods produced best results at Δε = 0. (iii) For ε greater than 0.94, all these three methods yield worst RMSE at Δε = 0.03. Equations (9) and (10) obtain better accuracy than Equations (1) and (13) when Δε = −0.02 and △ε = 0.03. The best accuracies obtained using these three methods are similar, with about 0.6 K at ε = 0.98 and Δε = 0. These results indicate that the quadratic equation between $T_s - T_i$ and $T_i - T_j$ works well for high emissivities close to one in both channels but performs poorly for low emissivities. For low emissivities, the developed algorithm has an obvious advantage. The greatest improvement of Equations (9) and (10) occurs at ε = 0.90 and Δε = −0.02, with a RMSE of 0.85 K, compared with the value of 1.71 K obtained by Equation (1) and the one of 1.41 by Equation (13).

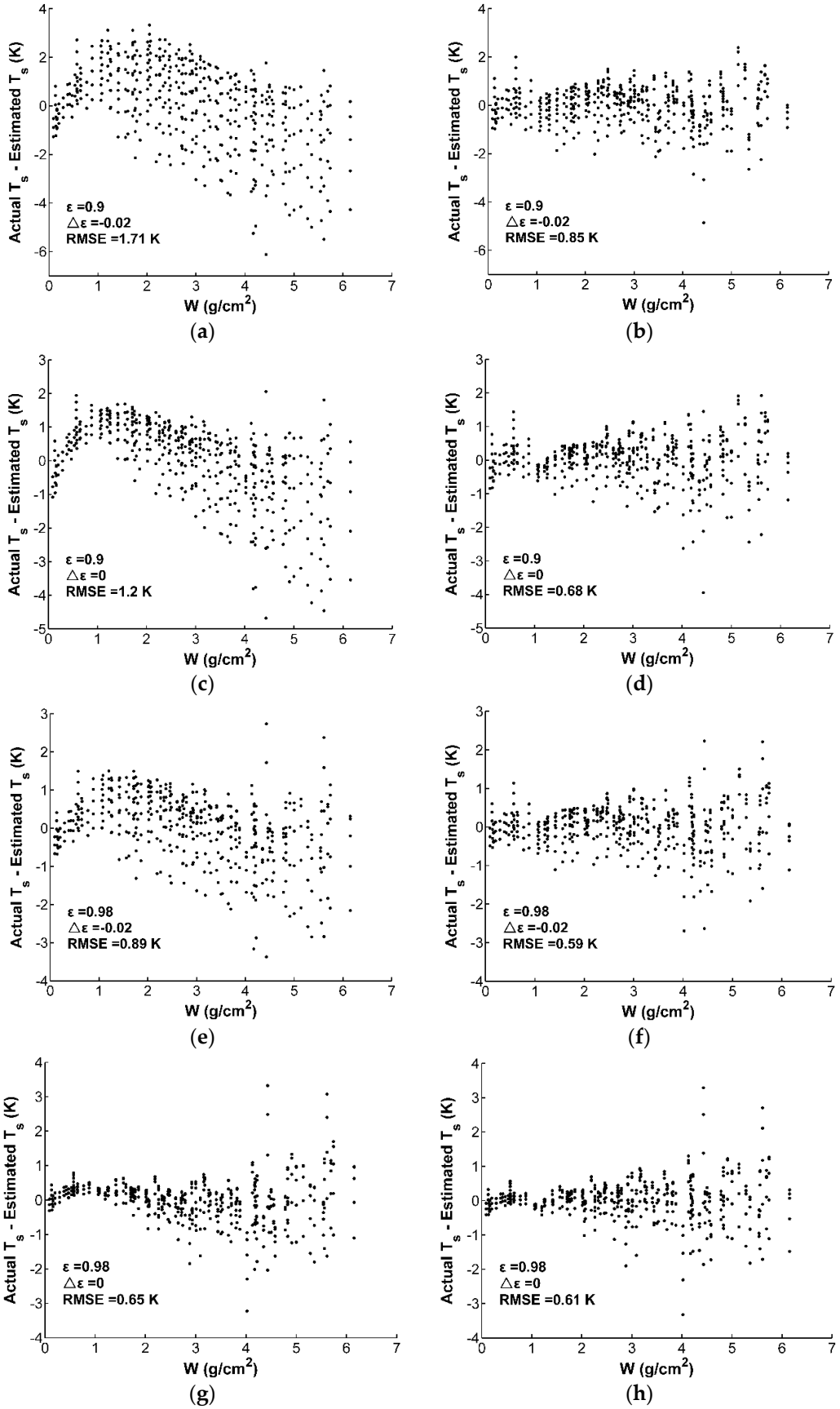


**Figure 13.** Comparison of the residuals related to Equation (1) (**a**,**c**,**e**,**g**) and Equations (9) and (10) (**b**,**d**,**f**,**h**) for different combinations of channel mean emissivity ($\varepsilon$) and channel emissivity difference ($\Delta\varepsilon$).

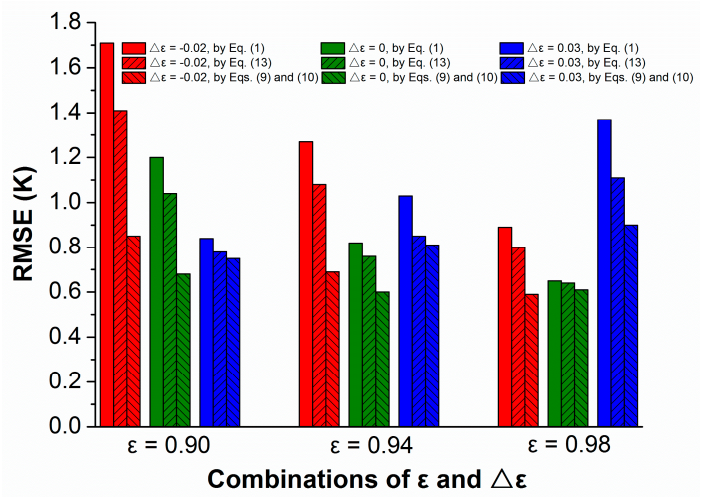


**Figure 14.** Comparison of RMSEs yielded by Equations (1) (9), (10) and (13) for different combinations of channel mean emissivity (ε) and channel emissivity difference (Δε).

### *4.2. Validation Using the Simulation Data*

Validation is necessary to understand how well the LST retrieved using the algorithm matches the actual one. The best method for algorithm validation is to compare the LST estimated from the satellite data with ground measurement. Because GF-5 satellite data is not available at the time of writing, testing the developed algorithm (Equations (11) and (12)) was done using simulation with another set of atmospheric profile data, TIGR_28. Figure 15 presents the error distribution between the actual and estimated LSTs, with RMSE = 0.67 K and bias = 0.09 K.

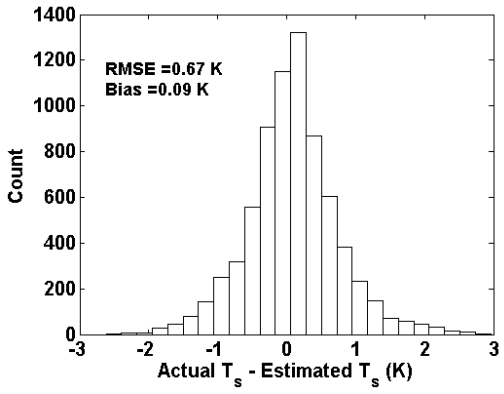


**Figure 15.** Histogram of the error between the actual LST and the estimation using Equations (11) and (12).

### *4.3. Sensitivity Analysis*

There are three main error sources for the determination of LST using Equations (11) and (12). The first is the instrument's performance, which yields error in the brightness temperatures. The second is the uncertainty in the LSE and the third originates from the determination error of atmospheric W.

#### 4.3.1. Instrument Noise

The accuracy of the estimated LST essentially depends on the radiometric performance of the instrument. The NEΔT of the infrared channels of the MSI onboard the GF-5 satellite is designed to be 0.2 K. To evaluate the sensitivity of Equations (11) and (12) to NEΔT, a simulation of the effect of instrument noise was performed using a set of randomly generated signal level perturbations with

errors of 0.1 K, 0.2 K and 0.3 K for both channels. The RMSEs between the true LSTs and those retrieved from the noise-added brightness temperatures are 0.83 K, 1.14 K and 1.51 K for NE$\Delta$T = 0.1 K, 0.2 K and 0.3 K, respectively, in both channels. In contrast to the RMSE of 0.70 K for noise-free cases, the retrieval accuracies are changed by 0.13 K, 0.44 K, and 0.81 K for NE$\Delta$T = 0.1 K, 0.2 K and 0.3 K, respectively. The results indicate that a NE$\Delta$T of more than 0.2 K in the infrared channels of the MSI onboard the GF-5 satellite can yield the relative large error for LST retrieval.

#### 4.3.2. Land Surface Emissivity

According to Equations (11) and (12), one can see that the LST retrieval accuracy related to LSE mainly depends on the uncertainties in $(1 - \varepsilon)$ and $\Delta\varepsilon$. If the reference errors of 1% in $(1 - \varepsilon)$ and $\Delta\varepsilon$ are considered, the RMSE due to the uncertainties in $(1 - \varepsilon)$ and $\Delta\varepsilon$ is 0.83 K, a change of 0.13 K from the error related to no uncertainties in $(1 - \varepsilon)$ and $\Delta\varepsilon$.

#### 4.3.3. Atmospheric Water Vapour Content

The W is not easily estimated from satellite measurements. It is necessary to evaluate the effect of the uncertainty in W on LST retrieval. In this work, the differences between the actual LSTs and those determined with 10%, 15% and 20% uncertainties in W were calculated. The RMSEs are 0.73 K, 0.76 K and 0.81 K for 10%, 15% and 20% uncertainties in W, respectively. These results indicate that the algorithm (Equations (11) and (12)) is not sensitive to the determination error of W.

#### 4.3.4. Total Error

Given the instrument noise and the uncertainties in LSE and atmospheric W, the total errors (RMSEs) of LST retrieval using Equations (11) and (12) are listed in Table 5 for different NE$\Delta$Ts and uncertainties in W, under the assumption of 1% uncertainties in $(1 - \varepsilon)$ and $\Delta\varepsilon$. The RMSE with NE$\Delta$T = 0.2 K, 1% uncertainties in $(1 - \varepsilon)$ and $\Delta\varepsilon$ and 20% uncertainty in W is 1.29 K. In contrast to the error of 0.70 K related to the algorithm itself, the LST retrieval accuracy is changed by 0.59 K, 64.7% from the instrument noise, 19.1% from the uncertainty in LSE and 16.2% from the uncertainty in W. The results indicate that instrument noise plays a major role in the LST retrieval error, assuming 1% uncertainties in $(1 - \varepsilon)$ and $\Delta\varepsilon$.

**Table 5.** The total RMSEs (K) related to different NE$\Delta$Ts and uncertainties in W, assuming 1% uncertainties in $(1 - \varepsilon)$ and $\Delta\varepsilon$.

| NE$\Delta$T (K) | Uncertainty in W | | |
|---|---|---|---|
| | 10% | 15% | 20% |
| 0.1 | 0.97 | 0.99 | 1.03 |
| 0.2 | 1.25 | 1.26 | 1.29 |
| 0.3 | 1.60 | 1.61 | 1.63 |

## 5. Application to ASTER Data

### *5.1. Study Area*

To evaluate the performance of the developed algorithm applied to the satellite data, we have chosen ASTER data based on its high resolution finer than 100 m for TIR bands. Two study areas (A and B), in which the geographic and climate conditions are different, were considered, as shown in Figure 16. Study area A is located in North China, covering the range from about 39°30′N to 40°05′N latitude and 116°5′E to 116°50′E longitude. This area has a typical monsoon climate characterized by hot and rainy summer, cold and dry winter. The land surface types are mainly farmland, urban and forest. Study area B, with about 49°50′N to 50°30′N latitude and 120°20′E to 121°10′E longitude, is located in Inner Mongolia, China. It has a temperate continental climate, i.e., low annual rainfall

amount and large annual temperature range. The land covers mainly include forest, farmland, town and bare land.

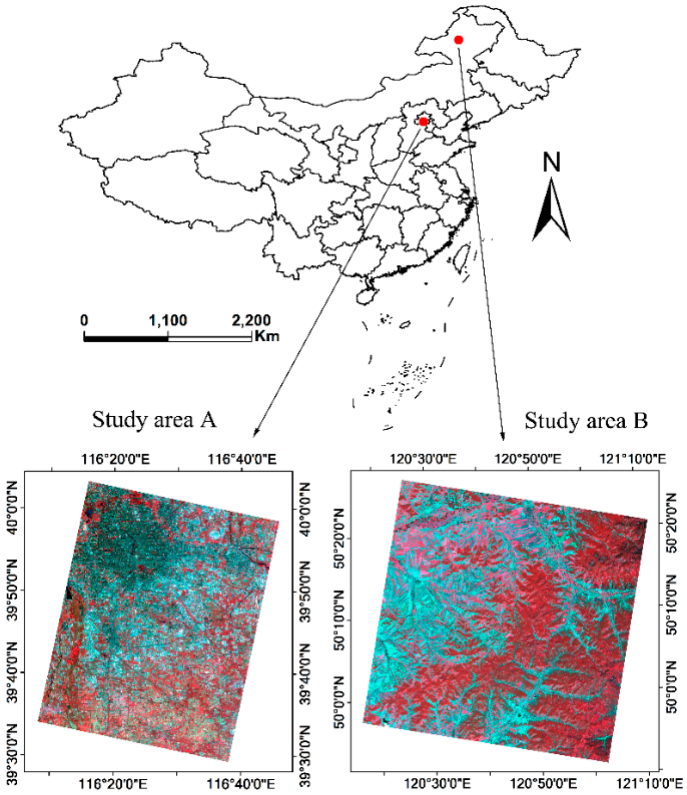


**Figure 16.** The study areas.

## 5.2. Data Processing

The satellite imagery used for study area A was recorded on 10 October, 2016 and for study area B recorded on 20 June, 2015. Considering that the developed algorithm is not sensitive to the determination error of W, MOD 05 precipitable water product was resampled to 90-m resolution using the nearest-neighbor interpolation method. After the data quality checking for all data, the geographic coordinate matching and temporal matching between ASTER and MOD 05, the images with 613 × 485 pixels for study area A and 619 × 625 pixels for study area B were used.

Considering the difference of the spectral response functions between the GF-5 and ASTER data, the coefficients in Equations (11) and (12), given in Table 6, were recalculated using the spectral response function of ASTER TIR data, with the RMSE of 0.69 K.

**Table 6.** Coefficients in Equation (9) for ASTER SW channels.

| Equation (11) | | Equation (12) | |
|---|---|---|---|
| $A$ | 0.6346 | $A$ | 0.6346 |
| $B$ | 4.302 | $B$ | 4.302 |
| | | $C_{111}$ | 0.2816 |
| | | $C_{112}$ | −1.0347 |
| | | $C_{a1}$ | −1.222 |
| | | $C_{a2}$ | −1.96 |
| $C_{m1}$ | 23.52 | $C_{b1}$ | −83.94 |
| $C_{m2}$ | −51.6 | $C_{b2}$ | 386.3 |
| $C_{n1}$ | 20.6 | $C_{c1}$ | 51.0 |
| $C_{n2}$ | −235 | $C_{c2}$ | −377 |
| $C_o$ | 0.18 | $C_d$ | 0.06 |

### *5.3. Results*

Using the coefficients in Table 6, the LST was estimated from ASTER L1B data. The histograms of the difference between AST 08 and the estimation using Equations (11) and (12) were displayed in Figure 17. Compared with AST 08, the proposed method underestimated the LST, with a RMSE of 0.86 K and a bias of 0.81 K for study area A and a RMSE of 0.83 K and a bias of 0.72 K for study area B. Therefore, the difference between AST 08 and the retrieved LST using Equations (11) and (12) is small, indicating that Equations (11) and (12) can be used for retrieving LST from GF-5 TIR data with the satisfactory accuracy.

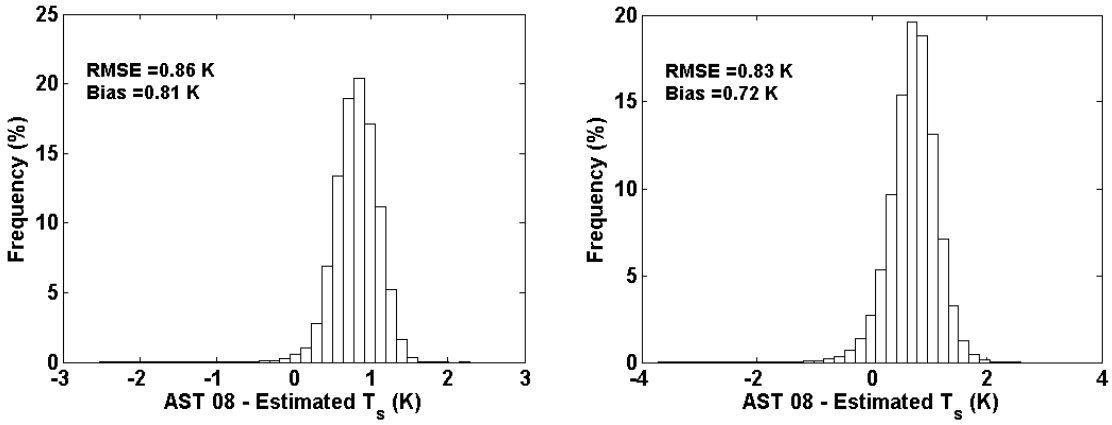


**Figure 17.** Histograms ((**a**) for study area A and (**b**) for study area B) of the difference between AST 08 and the estimated LST from ASTER L1B data using Equations (11) and (12).

## 6. Discussion

The quadratic expression in terms of $T_s - T_i$ and $T_i - T_j$ for LST retrieval received considerable attention due to its simplicity and the advantage of using the TOA brightness temperatures in two channels only. The quadratic method was proposed because the variation of the linear SW coefficient with the atmospheric situation can be approximately corrected by $T_i - T_j$ [15]. If W is disregarded, the quadratic SW method is a good choice for correcting the atmospheric effect for high emissivity but not for low emissivity.

For a given emissivity, the developed algorithm of Equations (9) and (10) that parameterized constant $C$ in the quadratic SW method improves the LST retrieval accuracy, especially for low emissivity. Based on Equations (9) and (10), an algorithm with coefficients incorporating the emissivity, i.e., Equations (11) and (12) was developed. Parameterizing constant $C$ led to the introduction of the atmospheric W into the LST retrieval algorithm. Despite the difficulty in determining W accurately, the sensitivity analysis of the uncertainty in W shows that if the error in W is 20%, the error in the LST estimation is still satisfactory, with a RMSE of 0.81 K. Notably, the main error of LST retrieval comes from instrument noise. Compared with Sobrino's algorithm that uses W and was also developed based on the quadratic SW method, the algorithm presented in this study gives improved accuracy. A disadvantage of the presented algorithm is the different expressions for different W groups (0–1.2 g/cm$^2$ and 0.8–6.5 g/cm$^2$), which increases the complexity of the algorithm.

Using ASTER L1B data as a proxy to test the presented algorithm, the proposed algorithm underestimated LST by about 0.8 K, compared with AST 08 product. This difference may be related to the different atmospheric correct methods. AST 08 was generated using the TES algorithm, in which the accurate atmospheric correct is needed for each band. The proposed algorithm was based on the SW method, which uses different absorptions of two channels to eliminate the atmospheric effects. One may note that there is a difference between the spectral response functions of the SW

channels for GF-5 and ASTER instruments, as shown in Figure 1. The coefficients in Equations (11) and (12) given in Tables 4 and 6 are therefore different for these two instruments, but the LST errors resulted from the algorithm itself are nearly the same (RMSE = 0.70 K for GF-5, RMSE = 0.69 K for ASTER) as shown in Sections 4.1 and 5.2 if the appropriate coefficients are used in Equations (11) and (12). It should be also noticed that except for the brightness temperatures measured by the two SW channels, other input parameters (emissivities and W) have to be provided in Equations (11) and (12) to retrieve LST. For generating operationally LST product with GF-5 data, the emissivities and W in Equations (11) and (12) will be estimated from GF-5 data using the NDVI-based threshold method [32] and the covariance-variance method [33], respectively.

Notably, compared with other atmospheres with similar W, the atmospheric profiles with W = 4.02 g/cm$^2$, W = 4.43 g/cm$^2$ and W = 5.61 g/cm$^2$ lead to relatively large errors (approximately 3 K) in both Equations (1), (9) and (10), as shown in Figure 13g,h. This may be related to the vertical distribution of water vapour in the atmosphere or the contribution of the other atmospheric constituents to LST retrieval. The details of this assumption can be analysed in future work.

## 7. Conclusions

The quadratic relationship expressed by $T_s - T_i = A\,(T_i - T_j)^2 + B\,(T_i - T_j) + C$ works for high emissivities in both channels. When the emissivity becomes small, does such an equation perform well with satisfactory accuracy? This study first checked the performance of the quadratic SW method for different emissivities. Unfortunately, when the emissivity was low, the quadratic relationship between $T_s - T_i$ and $T_i - T_j$ deteriorated and thus led to a RMSE of up to 1.71 K. To solve this problem, the constant $C$ was investigated for the emissivity combination of $\varepsilon = 0.90$ and $\Delta\varepsilon = -0.02$, which gave the worst result in the quadratic SW equation. In this procedure, the coefficients $A$ and $B$ were set to 0.2809 and 1.447, obtained for a black body. Based on the observation that $C$ was associated with W for W < 1 g/cm$^2$ and with both $T_0$ and W for W > 1 g/cm$^2$, an equation that parameterized this constant was created. Following this approach, an operational algorithm, i.e., Equations (11) and (12) were proposed. This algorithm worked correctly on the simulations and yielded a RMSE of 0.70 K. The inter-comparison with AST 08 product showed that the proposed algorithm underestimated LST by about 0.8 K for both study areas when applied to ASTER L1B data.

Sensitivity analyses were performed for the instrument noise and the uncertainties in atmospheric W and LSE. Given NE$\Delta$T = 0.2 K, a 20% uncertainty in W and 1% uncertainties in $(1 - \varepsilon)$ and $\Delta\varepsilon$, the calculated result had a RMSE of 1.29 K. In contrast to the RMSE of 0.70 K related to the algorithm itself, the LST retrieval accuracy was changed by 0.59 K, 64.7% from the instrument noise, 19.1% from the uncertainty in LSE and 16.2% from the uncertainty in W.

The originality of this work lies in (i) the proposal of a different algorithm for LST retrieval and (ii) addressing the lack of an algorithm for the coming generation of GF-5 data.

**Acknowledgments:** We thank the anonymous reviewers for their constructive suggestions and comments, from which this paper has greatly benefited. The author Yuanyuan Chen would like to thank the China Scholarship Council for the financial support of her stay in ICube (UMR7357), France. This work was funded by National High-resolution Earth Observation Project (11-Y20A32-9001-15/17) and the National Natural Science Foundation of China (41501406 and 41231170).

**Author Contributions:** Yuanyuan Chen wrote the manuscript and was in charge of the research design and data simulations. Zhao-Liang Li and Si-Bo Duan conceived of and designed the research. Huazhong Ren and Jelila Labed analyzed the simulated results.

**Conflicts of Interest:** The authors declare no conflict of interest.

## References

1. Li, Z.-L.; Tang, R.; Wan, Z.; Bi, Y.; Zhou, C.; Tang, B.; Yan, G.; Zhang, X. A review of current methodologies for regional evapotranspiration estimation from remotely sensed data. *Sensors* **2009**, *9*, 3801–3853. [CrossRef] [PubMed]

2. Torrion, J.; Maas, S.; Guo, W.; Bordovsky, J.; Cranmer, A. A three-dimensional index for characterizing crop water stress. *Remote Sens.* **2014**, *6*, 4025–4042. [CrossRef]
3. Goodin, D.G. Evaluation of a combined modelling-remote sensing method for estimating net radiation in a wetland: A case study in the Nebraska Sand Hills, U.S.A. *Int. J. Remote Sens.* **1995**, *16*, 1481–1494. [CrossRef]
4. Sandholt, I.; Rasmussen, K.; Andersen, J. A simple interpretation of the surface temperature/vegetation index space for assessment of surface moisture status. *Remote Sens. Environ.* **2002**, *79*, 213–224. [CrossRef]
5. Cammalleri, C.; Vogt, J. On the role of land surface temperature as proxy of soil moisture status for drought monitoring in Europe. *Remote Sens.* **2015**, *7*, 16849–16864. [CrossRef]
6. Duan, S.-B.; Li, Z.-L.; Tang, B.-H.; Wu, H.; Tang, R. Generation of a time-consistent land surface temperature product from MODIS data. *Remote Sens. Environ.* **2014**, *140*, 339–349. [CrossRef]
7. Wang, L.; Koike, T.; Yang, K.; Yeh, P.J.-F. Assessment of a distributed biosphere hydrological model against streamflow and MODIS land surface temperature in the upper Tone River Basin. *J. Hydrol.* **2009**, *377*, 21–34. [CrossRef]
8. Tateishi, R.; Ahn, C.H. Mapping evapotranspiration and water balance for global land surfaces. *ISPRS J. Photogramm. Remote Sens.* **1996**, *51*, 209–215. [CrossRef]
9. Weng, Q. Thermal infrared remote sensing for urban climate and environmental studies: Methods, applications, and trends. *ISPRS J. Photogramm. Remote Sens.* **2009**, *64*, 335–344. [CrossRef]
10. Wan, Z.; Wang, P.; Li, X. Using MODIS land surface temperature and normalized difference vegetation index products for monitoring drought in the southern Great Plains, USA. *Int. J. Remote Sens.* **2004**, *25*, 61–72. [CrossRef]
11. Goward, S.N.; Xue, Y.; Czajkowski, K.P. Evaluating land surface moisture conditions from the remotely sensed temperature vegetation index measurements: An exploration with the simplified simple biosphere model. *Remote Sens. Environ.* **2002**, *79*, 225–242. [CrossRef]
12. Marques da Silva, J.R.; Damásio, C.V.; Sousa, A.M.O.; Bugalho, L.; Pessanha, L.; Quaresma, P. Agriculture pest and disease risk maps considering MSG satellite data and land surface temperature. *Int. J. Appl. Earth Obs. Geoinf.* **2015**, *38*, 40–50. [CrossRef]
13. Sobrino, J.A.; Caselles, V.; Coll, C. Theoretical split-wimdow algorithms for determining the actual surface temperature. *Il Nuovo Cimento C* **1993**, *16*, 219–236. [CrossRef]
14. Becker, F.; Li, Z.-L. Towards a local split window method over land surfaces. *Int. J. Remote Sens.* **1990**, *11*, 369–393. [CrossRef]
15. Coll, C.; Caselles, V.; Sobrino, J.A.; Valor, E. On the atmospheric dependence of the split-window equation for land surface temperature. *Int. J. Remote Sens.* **1994**, *15*, 105–122. [CrossRef]
16. Jiménez-Muñoz, J.C.; Sobrino, J.A. A generalized single-channel method for retrieving land surface temperature from remote sensing data. *J. Geophys. Res.* **2003**, *108*, 4688–4698. [CrossRef]
17. Wan, Z.; Dozier, J. A generalized split-window algorithm for retrieving land-surface temperature from space. *IEEE Trans. Geosci. Remote Sens.* **1996**, *34*, 892–905.
18. Gillespie, A.; Rokugawa, S.; Matsunaga, T.; Cothern, J.S.; Hook, S.; Kahle, A.B. A temperature and emissivity separation algorithm for Advanced Spaceborne Thermal Emission and Reflection Radiometer (ASTER) Images. *IEEE Trans. Geosci. Remote Sens.* **1998**, *36*, 1113–1126. [CrossRef]
19. Lu, L.; Venus, V.; Skidmore, A.; Wang, T.; Luo, G. Estimating land-surface temperature under clouds using MSG/SEVIRI observations. *Int. J. Appl. Earth Obs. Geoinf.* **2011**, *13*, 265–276. [CrossRef]
20. Li, Z.-L.; Tang, B.-H.; Wu, H.; Ren, H.; Yan, G.; Wan, Z.; Trigo, I.F.; Sobrino, J.A. Satellite-derived land surface temperature: Current status and perspectives. *Remote Sens. Environ.* **2013**, *131*, 14–37. [CrossRef]
21. Gillespie, A.R.; Abbott, E.A.; Gilson, L.; Hulley, G.; Jiménez-Muñoz, J.-C.; Sobrino, J.A. Residual errors in ASTER temperature and emissivity standard products AST08 and AST05. *Remote Sens. Environ.* **2011**, *115*, 3681–3694. [CrossRef]
22. Hulley, G.C.; Hook, S.J.; Baldridge, A.M. ASTER land surface emissivity database of California and Nevada. *Geophys. Res. Lett.* **2008**, *35*, L13401. [CrossRef]
23. Coll, C.; Caselles, V. A split-window algorithm for land surface temperature from advanced very high resolution radiometer data: Validation and algorithm comparison. *J. Geophys. Res.* **1997**, *102*, 16697–16713. [CrossRef]
24. Sobrino, J.A.; Raissouni, N. Toward remote sensing methods for land cover dynamic monitoring: Application to Morocco. *Int. J. Remote Sens.* **2000**, *21*, 353–366. [CrossRef]

25. François, C.; Ott1é, C. Atmospheric corrections in the thermal infrared: Global and water vapor dependent split-window algorithms-Applications to ATSR and AVHRR data. *IEEE Trans. Geosci. Remote Sens.* **1996**, *34*, 457–470. [CrossRef]
26. Sun, D.; Pinker, R.T. Estimation of land surface temperature from a Geostationary Operational Environmental Satellite (GOES-8). *J. Geophys. Res.* **2003**, *108*, 4326. [CrossRef]
27. Becker, F. The impact of spectral emissivity on the measurement of land surface temperature from a satellite. *Int. J. Remote Sens.* **1987**, *8*, 1509–1522. [CrossRef]
28. Scott, N.A.; Chédin, A. A fast line-by-line method for atmospheric absorption computations: The automatized atmospheric absorption atlas. *J. Appl. Meteorol.* **1981**, *20*, 802–812. [CrossRef]
29. Berk, A.; Anderson, G.P.; Acharya, P.K.; Chetwynd, J.H.; Bernstein, L.S.; Shettle, E.P.; Matthew, M.W.; Adler-Golden, S.M. *MODTRAN4 User's Manual*; Air Force Research Laboratory: Hanscom AFB, MA, USA, 1999.
30. Sobrino, J.A.; Li, Z.-L.; Stoll, M.P.; Becker, F. Multi-channel and multi-angle algorithms for estimating sea and land surface temperature with ATSR data. *Int. J. Remote Sens.* **1996**, *17*, 2089–2114. [CrossRef]
31. Ulivieri, C.; Castronuovo, M.M.; Francioni, R.; Cardillo, A. A split window algorithm for estimating land surface temperatue from satellites. *Adv. Space Res.* **1994**, *14*, 59–65. [CrossRef]
32. Tang, B.H.; Shao, K.; Li, Z.L.; Wu, H.; Tang, R. An improved NDVI-based threshold method for estimating land surface emissivity using MODIS satellite data. *Int. J. Remote Sens.* **2015**, *36*, 4864–4878. [CrossRef]
33. Li, Z.-L.; Jia, L.; Su, Z.; Wan, Z.; Zhang, R. A new approach for retrieving precipitable water from ATSR2 split-window channel data over land area. *Int. J. Remote Sens.* **2003**, *24*, 5095–5117. [CrossRef]